Supplementary Information for *"Oscillator-qubit generalized quantum signal processing: a case study of uracil cation vibronic model"*

Jungsoo Hong,[1] Seong Ho Kim,[2] Seung Kyu Min,[2,*] and Joonsuk Huh[3,4,†]

[1] *SKKU Advanced Institute of Nano Technology (SAINT), Sungkyunkwan University, Suwon 16419, Republic of Korea*
[2] *Department of Chemistry, Ulsan National Institute of Science and Technology, Ulsan 44919, Republic of Korea*
[3] *Department of Chemistry, Yonsei University, Seoul 03722, Republic of Korea*
[4] *Department of Quantum Information, Yonsei University, Seoul 03722, Republic of Korea*

(Dated: April 21, 2026)

I. VALUES OF MOLECULAR NORMAL MODE PARAMETERS

Hamiltonian of the Uracil cation is built up based on the previous paper [1, 2]. Notice that typos in the tables are corrected based on the potential energy surface plots. The parameters of potentials and the harmonic frequencies ω_r are given in eV and cm^{-1}. For convenience, Table S.I summarizes the fitted linear and quadratic coupling parameters, Table S.II summarizes the quartic potentials, and Table S.III summarizes the Morse-potential parameters.

II. FAILURE OF QVC APPROXIMATION

The necessity of anharmonic terms becomes apparent when comparing the quadratic vibronic coupling (QVC) model against the full anharmonic model. Figure S1 reveals how the QVC approximation severely distorts the potential energy surfaces along critical vibrational coordinates,

TABLE S.I. Fitted Parameters: ω in cm^{-1}, $\kappa_i^{(\alpha)}$, $\lambda^{(\alpha\beta)}$ and $\gamma_{ii}^{(\alpha)}$ in eV for States D_0–D_3 ($\alpha = 0$–3) and Modes ν_3, ν_7, ν_{11}, ν_{18}–ν_{21} ($i = 3, 7, 11, 18$–21) [1]. Parameters of the first order diagonal term $\sum_r \kappa_r^{(n)} |n\rangle\langle n| \hat{Q}_r$, the first order off-diagonal term $\sum_i \lambda_i^{(nm)}(|m\rangle\langle n| + |n\rangle\langle m|)\hat{Q}_i$ and the quadratic coupling term $\frac{1}{2}\sum_{i,n} \gamma_i^{(n)} |n\rangle\langle n| \hat{Q}_i^2$ are tabulated.

Mode	ω	$\kappa^{(0)}$	$\kappa^{(1)}$	$\kappa^{(2)}$	$\kappa^{(3)}$	$\lambda^{(02)}$	$\lambda^{(13)}$	$\gamma^{(0)}$	$\gamma^{(1)}$	$\gamma^{(2)}$	$\gamma^{(3)}$
ν_3	388	0.04139	-0.02688	-0.05853	0.00132			0.00383	-0.00426	-0.00366	-0.00947
ν_7	560	-0.05367	-0.00503	0.00775	-0.04581	0.02141					
ν_{11}	770	0.05357	-0.02456	0.03697	-0.02130	0.02082	0.01845				
ν_{18}	1193	-0.02203	0.09074	0.02748	-0.04054	-0.03538	0.08077	0.01938	0.00694	-0.00294	0.00752
ν_{19}	1228	0.07472	-0.00582	0.00889	-0.02136	-0.03763	0.05834	0.01590	0.01348	0.00901	0.00497
ν_{20}	1383	-0.12147	0.05316	0.11233	0.00747	-0.02049		0.01489	0.00828	0.00183	0.00546
ν_{21}	1406	-0.09468	0.04454	0.14539	0.00050		0.07284	0.00970	0.00096	-0.00114	0.01108

* skmin@unist.ac.kr
† joonsukhuh@yonsei.ac.kr

TABLE S.II. Quartic potentials $\frac{1}{24}k_r^{(a)}\hat{Q}_r^4$ [1].

Mode	ω	$k^{(0)}$	$k^{(1)}$	$k^{(2)}$	$\lambda^{(01)}$	$\lambda^{(12)}$
ν_{10}	734	0.03317	0.01157	0.01534	0.04633	0.03148
ν_{12}	771	0.02979	0.01488	0.01671	0.03540	0.03607

TABLE S.III. Morse Potentials $V_k^{(\alpha)}(\hat{Q}_k) = d_k^{(\alpha)}[\mathrm{e}^{(a_k^{(\alpha)})(\hat{Q}_k - q_{k,0}^{(\alpha)})} - 1]^2 + e_0^{(\alpha)}$

Mode state	ω	d_0	a	q_0	e_0	$\lambda^{(02)}$	$\lambda^{(13)}$
ν_{24}	1673						-0.01832
D_0		41.89704	-0.04719	0.81440	-0.06431		
D_1		38.37122	-0.05231	0.37488	-0.01505		
D_2		39.25691	-0.05286	0.14859	-0.00244		
D_3		37.97847	-0.05431	-0.18152	-0.00366		
ν_{25}	1761					0.00114	0.12606
D_0		4.80270	0.13675	0.02883	-0.00007		
D_1		74.15995	0.03064	-1.34468	-0.12082		
D_2		90.76928	0.03374	-0.29923	-0.00916		
D_3		20.56079	0.08044	0.38841	-0.02071		
ν_{26}	1794					0.13035	0.14272
D_0		22.92802	-0.07438	-0.32069	-0.01274		
D_1		18.27440	-0.07911	-0.01711	-0.00003		
D_2		9.46894	-0.08653	0.37635	-0.01037		
D_3		65.09678	-0.03660	1.66312	-0.25639		

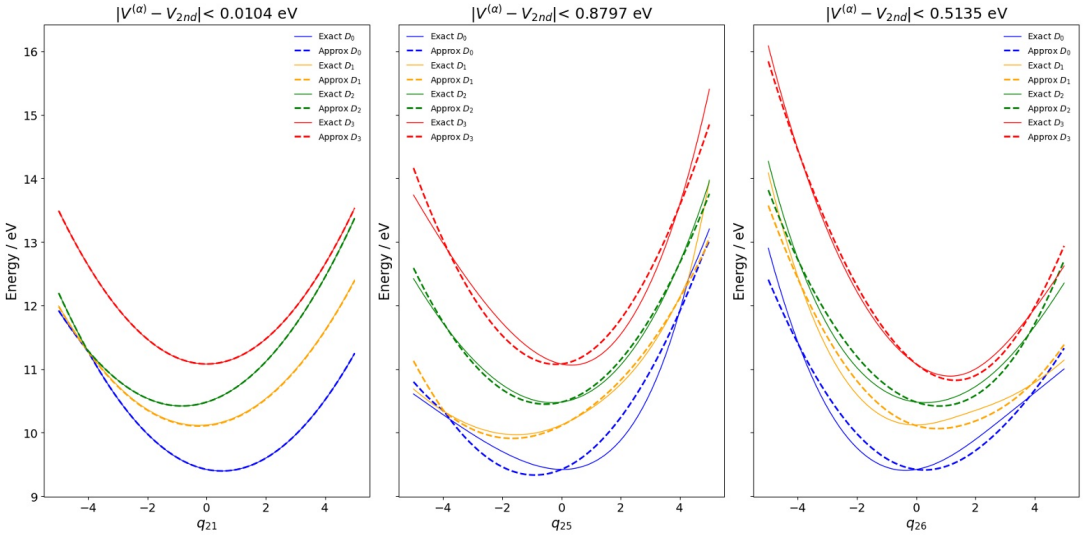

FIG. S1. Potential-energy cuts along 3 energy-dominant modes ν_{21}, ν_{25} and ν_{26} coordinate. The QVC model can misplace the CIs by > 0.3 eV.

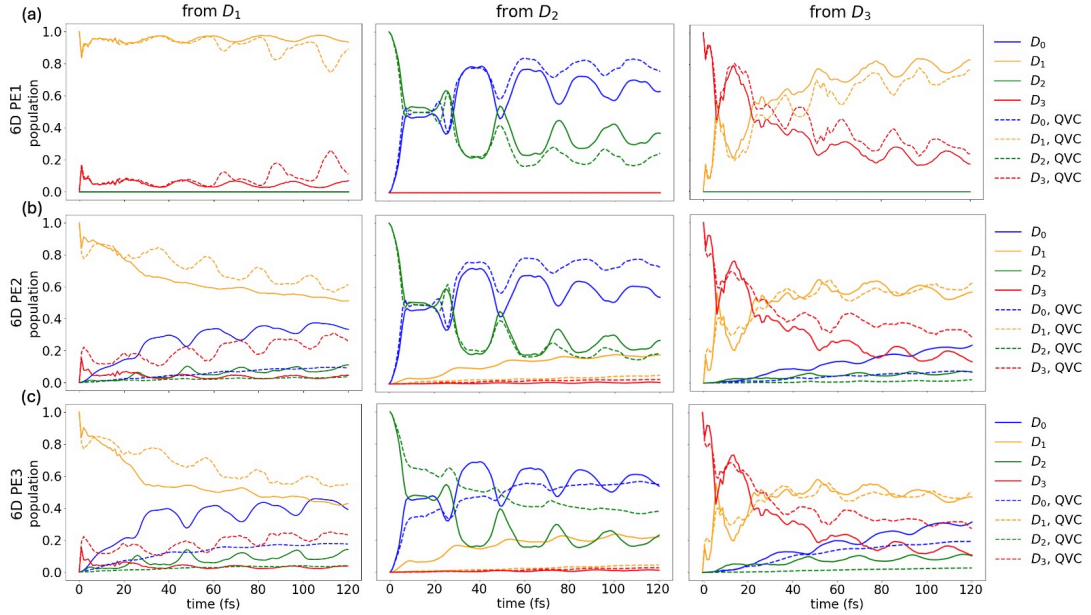

FIG. S2. MCTDH population dynamics for different mode set 6D PE1-3 and initial states D_1-D_3. Only the anharmonic model reproduces the ultrafast ≤ 50 fs oscillating relaxation.

misplacing CIs along the ν_{25} and ν_{26} carbonyl stretch by more than 0.3 eV. These errors propagate to the dynamics. Figure S2 compares MCTDH population dynamics for initial excitation into the D_2 state. The anharmonic model predicts complete depopulation within 50 femtoseconds—consistent with experimental observations—while the QVC model fails to capture the rapid relaxation through the conical intersection. Since QVC already includes second-order diagonal corrections and is therefore strictly more accurate than the linear vibronic coupling (LVC) approximation, its failure to reproduce the anharmonic dynamics reveals the essential role of higher-order diagonal anharmonicity near the CI seam.

We compare the exact model with the QVC model, not with the LVC model, because the phase-space rotation gates $R_{nr}(\theta) = \exp\left[-\mathrm{i}\theta\hat{\sigma}_z\hat{a}_r^\dagger\hat{a}_r\right]$ enable native implementation upto quadratic potentials. Trapped-ion systems realize these through state-dependent squeezing, where driving at twice the motional frequency generates spin-dependent coordinate transformations in phase space [3]. In circuit QED, the dispersive interactions between the bosonic mode and the auxiliary qubit realize a spin-dependent phase space rotation gate [4].

III. OQ-GQSP: CONSTRUCTION DETAILS AND APPROXIMATION BOUNDS

A. Signal operator decomposition

The key building block is the OQ-GQSP signal operator construction introduced in the main text. Here we give its explicit gate decomposition. On trapped-ion [5] and circuit-QED [4, 6] platforms, both the Z-basis controlled displacement $\mathrm{CD}_z(\xi) = e^{i\xi\hat{\sigma}_z\hat{Q}}$ and the unconditional displacement

$D(\xi) = e^{i\xi\hat{Q}}$ are native operations. The signal operator $A_{\hat{Q}} = \mathrm{diag}(\hat{U}, \mathbb{I}_{\mathrm{osc}})$ with $\hat{U} = e^{i\pi\hat{Q}/L}$ is then constructed *without ancilla qubits* by a single pair of displacements:

$$\mathrm{CD}_z\left(\tfrac{\pi}{2L}\right) \cdot D\left(\tfrac{\pi}{2L}\right) = \begin{bmatrix} \mathrm{e}^{\mathrm{i}\frac{\pi}{2L}\hat{Q}} & 0 \\ 0 & \mathrm{e}^{-\mathrm{i}\frac{\pi}{2L}\hat{Q}} \end{bmatrix} \begin{bmatrix} \mathrm{e}^{\mathrm{i}\frac{\pi}{2L}\hat{Q}} & 0 \\ 0 & \mathrm{e}^{\mathrm{i}\frac{\pi}{2L}\hat{Q}} \end{bmatrix} = \begin{bmatrix} \mathrm{e}^{\mathrm{i}\frac{\pi}{L}\hat{Q}} & 0 \\ 0 & \mathbb{I}_{\mathrm{osc}} \end{bmatrix} = A_{\hat{Q}}. \tag{S1}$$

The $|0\rangle_q$ component acquires displacement $e^{i(\pi/2L+\pi/2L)\hat{Q}} = \hat{U}$, while the $|1\rangle_q$ component sees $e^{i(-\pi/2L+\pi/2L)\hat{Q}} = \mathbb{I}_{\mathrm{osc}}$. The complementary operator $B_{\hat{Q}} = \mathrm{diag}(\mathbb{I}_{\mathrm{osc}}, \hat{U}^\dagger)$ is obtained analogously via $D(-\pi/2L) \cdot \mathrm{CD}_z(\pi/2L)$. With $A_{\hat{Q}}$ and $B_{\hat{Q}}$, the GQSP circuit [7] interleaves these signal operators with single-qubit rotations to produce

$$\text{OQ-GQSP} = \begin{pmatrix} F(\hat{U}) & -(G(\hat{U}))^\dagger \\ G(\hat{U}) & (F(\hat{U}))^\dagger \end{pmatrix}, \tag{S2}$$

where $F(\hat{U}) = \sum_{n=-d}^{d} c_n \mathrm{e}^{\mathrm{i}n\pi\hat{Q}/L}$ is a degree-d Fourier series (equivalently, a Laurent polynomial in $e^{i\pi Q/L}$) satisfying the standard GQSP admissibility condition on the unit circle, e.g. $\sup_{|z|=1} |F(z)| \leq 1$, so that a complementary $G(z)$ exists with $|F(z)|^2 + |G(z)|^2 = 1$ for $|z| = 1$.

B. State-dependent nonlinear bosonic phase gate

We now add state-selectivity to OQ-GQSP, enabling its use in multi-state vibronic simulation. A subtle point is that OQ-GQSP requires mid-circuit measurements on an ancilla qubit, which could collapse the electronic-state superposition encoded in the main qubits. We resolve this by adapting a measurement-based phase-injection protocol: the nonlinear bosonic phase is 'injected' onto a single target electronic state via parity measurements that herald success without disturbing the remaining electronic-state population. This is analogous to gate teleportation of non-Clifford gates, where a non-trivial phase is imprinted through measurement, completing the ISA for multi-state anharmonic vibronic simulation.

Lemma 1 (OQ-GQSP to state-dependent nonlinear bosonic phase gate)**.** Given a state in oscillator-qubit processor $|\psi_D\rangle |\mathrm{osc}\rangle |0\rangle_a$ with four inverted-unary-encoded electronic states $|\psi_D\rangle$, an oscillator $|\mathrm{osc}\rangle$, and an ancilla qubit $|0\rangle_a$, we can approximately implement a target-state nonlinear bosonic phase gate $\mathrm{e}^{i|D_n\rangle\langle D_n|V_{nr}(\hat{Q}_r)}$ using two OQ-GQSP operators and two heralded measurements. If each OQ-GQSP block has leakage weight bounded by $\delta := |G(\hat{U})|^2 \ll 1$ on the relevant subspace, then the total success probability is $(1-\delta)^2$, while the non-target branches undergo $F(\hat{U})^\dagger F(\hat{U}) = \mathbb{I} + \mathcal{O}(\delta)$.

Proof. Let

$$\begin{aligned} \text{OQ-GQSP}_a &= \begin{pmatrix} F(\hat{U}) & -(G(\hat{U}))^\dagger \\ G(\hat{U}) & (F(\hat{U}))^\dagger \end{pmatrix}_a \\ &= |0\rangle_a \langle 0|_a F(\hat{U}) - |0\rangle_a \langle 1|_a (G(\hat{U}))^\dagger + |1\rangle_a \langle 0|_a G(\hat{U}) + |1\rangle_a \langle 1|_a (F(\hat{U}))^\dagger \end{aligned} \tag{S3}$$

and

$$\begin{aligned} \text{OQ-GQSP}_m &= \begin{pmatrix} F(\hat{U}) & -(G(\hat{U}))^\dagger \\ G(\hat{U}) & (F(\hat{U}))^\dagger \end{pmatrix}_m \\ &= |0\rangle_m \langle 0|_m F(\hat{U}) - |0\rangle_m \langle 1|_m (G(\hat{U}))^\dagger + |1\rangle_m \langle 0|_m G(\hat{U}) + |1\rangle_m \langle 1|_m (F(\hat{U}))^\dagger. \end{aligned} \tag{S4}$$

The inverted-unary-encoded electronic state can be represented as $|\psi_D\rangle = a_0 |D_0\rangle + a_1 |D_1\rangle + a_2 |D_2\rangle + a_3 |D_3\rangle$, where $\sum_i |a_i|^2 = 1$. The protocol proceeds in five stages.

Stage 1: Phase injection on the ancilla. Applying OQ-GQSP$_a$ entangles the bosonic phase with the ancilla qubit while leaving the electronic superposition untouched:

$$|\psi_D\rangle |\text{osc}\rangle |0\rangle_a \xrightarrow{\text{OQ-GQSP}_a} |\psi_D\rangle \left(F(\hat{U}) |\text{osc}\rangle |0\rangle_a + G(\hat{U}) |\text{osc}\rangle |1\rangle_a\right). \tag{S5}$$

Stage 2: First heralded measurement. Measuring the ancilla in the $|0\rangle_a$ basis projects out the desired $F(\hat{U})$ branch, succeeding with probability $1 - \delta$:

$$\xrightarrow{\text{Measure } |0\rangle_a\langle 0|_a} |\psi_D\rangle F(\hat{U}) |\text{osc}\rangle |0\rangle_a \text{ with probability } \mathbf{1 - \delta}. \tag{S6}$$

Stage 3: State-selective phase doubling. A second OQ-GQSP$_m$ acts on the main qubit that encodes the target electronic state $|D_0\rangle = |1110\rangle$. Because the inverted-unary encoding places a $|0\rangle$ in the target qubit position only for $|D_0\rangle$, the F branch is applied to $|D_0\rangle$, the $F^\dagger$ branch to other odd-parity electronic states, and the G and $G^\dagger$ branches are located in even-parity code spaces:

$$\begin{aligned}
\xrightarrow{\text{OQ-GQSP}_m} & a_0 \left(|1110\rangle F(\hat{U})^2 |\text{osc}\rangle |0\rangle_a + |1111\rangle G(\hat{U})F(\hat{U}) |\text{osc}\rangle |0\rangle_a\right) \\
& a_1 \left(|1100\rangle (-G(\hat{U})^\dagger)F(\hat{U}) |\text{osc}\rangle |0\rangle_a + |1101\rangle F(\hat{U})^\dagger F(\hat{U}) |\text{osc}\rangle |0\rangle_a\right) \\
& a_2 \left(|1010\rangle (-G(\hat{U})^\dagger)F(\hat{U}) |\text{osc}\rangle |0\rangle_a + |1011\rangle F(\hat{U})^\dagger F(\hat{U}) |\text{osc}\rangle |0\rangle_a\right) \\
& a_3 \left(|0110\rangle (-G(\hat{U})^\dagger)F(\hat{U}) |\text{osc}\rangle |0\rangle_a + |0111\rangle F(\hat{U})^\dagger F(\hat{U}) |\text{osc}\rangle |0\rangle_a\right).
\end{aligned} \tag{S7}$$

Stage 4: Parity measurement. A parity measurement between the main qubit and the ancilla sorts the F^2 and $F^\dagger F$ branches into different ancilla states, without revealing which electronic state is occupied—this is the key step that protects the electronic superposition:

$$\begin{aligned}
\xrightarrow{\text{Parity measure}} & a_0 \left(|1110\rangle F(\hat{U})^2 |\text{osc}\rangle |1\rangle_a + |1111\rangle G(\hat{U})F(\hat{U}) |\text{osc}\rangle |0\rangle_a\right) \\
& a_1 \left(|1100\rangle (-G(\hat{U})^\dagger)F(\hat{U}) |\text{osc}\rangle |0\rangle_a + |1101\rangle F(\hat{U})^\dagger F(\hat{U}) |\text{osc}\rangle |1\rangle_a\right) \\
& a_2 \left(|1010\rangle (-G(\hat{U})^\dagger)F(\hat{U}) |\text{osc}\rangle |0\rangle_a + |1011\rangle F(\hat{U})^\dagger F(\hat{U}) |\text{osc}\rangle |1\rangle_a\right) \\
& a_3 \left(|0110\rangle (-G(\hat{U})^\dagger)F(\hat{U}) |\text{osc}\rangle |0\rangle_a + |0111\rangle F(\hat{U})^\dagger F(\hat{U}) |\text{osc}\rangle |1\rangle_a\right).
\end{aligned} \tag{S8}$$

Stage 5: Second heralded measurement and ancilla reset. Measuring $|1\rangle_a$ selects the successful branch. For the target state $|D_0\rangle$, the oscillator acquires $F(\hat{U})^2$; for all non-target states, $F^\dagger F \approx \mathbb{I}$ (by the GQSP unitarity constraint $|F|^2 + |G|^2 = 1$ with $\delta \ll 1$):

$$\begin{aligned}
\xrightarrow{\text{Measure } |1\rangle_a\langle 1|_a} & a_0 |1110\rangle F(\hat{U})^2 |\text{osc}\rangle |1\rangle_a + a_1 |1101\rangle F(\hat{U})^\dagger F(\hat{U}) |\text{osc}\rangle |1\rangle_a \\
& + a_2 |1011\rangle F(\hat{U})^\dagger F(\hat{U}) |\text{osc}\rangle |1\rangle_a + a_3 |0111\rangle F(\hat{U})^\dagger F(\hat{U}) |\text{osc}\rangle |1\rangle_a \\
& \quad \text{with probability } \mathbf{1 - \delta} \\
\approx & a_0 |1110\rangle F(\hat{U})^2 |\text{osc}\rangle |1\rangle_a + a_1 |1101\rangle |\text{osc}\rangle |1\rangle_a \\
& + a_2 |1011\rangle |\text{osc}\rangle |1\rangle_a + a_3 |0111\rangle |\text{osc}\rangle |1\rangle_a \\
\xrightarrow{\text{Reset ancilla } |0\rangle_a} & a_0 |1110\rangle F(\hat{U})^2 |\text{osc}\rangle |0\rangle_a + a_1 |1101\rangle |\text{osc}\rangle |0\rangle_a \\
& + a_2 |1011\rangle |\text{osc}\rangle |0\rangle_a + a_3 |0111\rangle |\text{osc}\rangle |0\rangle_a .
\end{aligned} \tag{S9}$$

The two heralded measurements yield a combined success probability of $(1-\delta)^2$. Crucially, the parity measurement (Stage 4) reveals only the parity—not which electronic state is occupied—so the electronic superposition $|\psi_D\rangle$ is preserved throughout. This approximately implements the desired state-dependent phase gate $e^{i|D_n\rangle\langle D_n|V_{nr}(\hat{Q}_r)}$ without collapsing the electronic-state data of the main qubits. □

C. Fourier-extension truncation bound

OQ-GQSP approximates nonlinear bosonic phase gates via truncated Fourier series. A natural question is: how many Fourier terms (i.e., what circuit depth d) are needed to achieve a target accuracy ε? The following lemma shows that for analytic potentials—which include all physically relevant cases such as polynomial, Morse, and trigonometric potentials—the Fourier coefficients decay *exponentially*, so only $d = \mathcal{O}(\ln \varepsilon^{-1})$ terms suffice.

Lemma 2 (Fourier-extension truncation for phase functions)**.** Let $I = [c-h, c+h]$ with $h > 0$, let $\tau > 1$, let $\varepsilon \in (0,1)$, and define

$$L_{\text{eff}} := \tau h.$$

Let $f : I \to \mathbb{R}$ be real-analytic and set

$$g(x) := e^{\mathrm{i}\Delta t f(x)}, \qquad x \in I.$$

Assume there exists a $2L_{\text{eff}}$-periodic function $g_{\text{ext}} : \mathbb{R} \to \mathbb{C}$ such that $g_{\text{ext}}(x) = g(x)$ for all $x \in I$, and g_{ext} admits a holomorphic extension to the strip of half-width $\sigma > 0$,

$$\mathcal{S}_\sigma := \{z \in \mathbb{C} : \ |\operatorname{Im} z| < \sigma\},$$

with

$$\sup_{z \in \mathcal{S}_\sigma} |g_{\text{ext}}(z)| \le B$$

for some $B \ge 1$. Write the Fourier series of the enlarged-period extension as

$$g_{\text{ext}}(x) = \sum_{k \in \mathbb{Z}} a_k \, e^{\mathrm{i}\frac{\pi k}{L_{\text{eff}}}(x-c)},$$

where

$$a_k = \frac{1}{2L_{\text{eff}}} \int_{c-L_{\text{eff}}}^{c+L_{\text{eff}}} g_{\text{ext}}(x) \, e^{-\mathrm{i}\frac{\pi k}{L_{\text{eff}}}(x-c)} \, dx.$$

Then, with

$$\rho_{\text{FE}} := e^{\pi\sigma/L_{\text{eff}}} > 1,$$

the coefficients satisfy

$$|a_k| \le B \, \rho_{\text{FE}}^{-|k|} \qquad (k \in \mathbb{Z}).$$

Hence the d-term Fourier-extension truncation

$$g_{(d)}^{\mathrm{FE}}(x) := \sum_{|k|\le d} a_k e^{\mathrm{i}\frac{\pi k}{L_{\mathrm{eff}}}(x-c)}$$

obeys

$$\|g - g_{(d)}^{\mathrm{FE}}\|_I \le \frac{2B\,\rho_{\mathrm{FE}}^{-(d+1)}}{1-\rho_{\mathrm{FE}}^{-1}} \le \varepsilon$$

provided

$$d \ge \left\lceil \frac{L_{\mathrm{eff}}}{\pi\sigma}\,\ln\!\Big(\frac{2B}{(1-\rho_{\mathrm{FE}}^{-1})\varepsilon}\Big)\right\rceil.$$

For fixed Δt, h, τ, and σ,

$$d = \mathcal{O}\big(\ln \varepsilon^{-1}\big).$$

The connection between strip analyticity and exponential decay of Fourier coefficients is classical [8]; the Fourier extension framework and its approximation-theoretic foundations are developed in Refs. [9–11].

Proof. Put $w := e^{\mathrm{i}\pi(z-c)/L_{\mathrm{eff}}}$; this maps $\mathcal{S}_\sigma$ conformally onto the annulus $\mathcal{A}_{\rho_{\mathrm{FE}}} := \{\rho_{\mathrm{FE}}^{-1} < |w| < \rho_{\mathrm{FE}}\}$ with $\rho_{\mathrm{FE}} = e^{\pi\sigma/L_{\mathrm{eff}}}$. Set $\tilde g(w) := g_{\mathrm{ext}}\big(c + \frac{L_{\mathrm{eff}}}{\mathrm{i}\pi}\log w\big)$, using the principal branch of log. Then $\tilde g$ is analytic on $\mathcal{A}_{\rho_{\mathrm{FE}}}$ and $|\tilde g(w)| \le B$ there.

By the change of variables $w = e^{\mathrm{i}\pi(x-c)/L_{\mathrm{eff}}}$ we have $dx = \frac{L_{\mathrm{eff}}}{\mathrm{i}\pi}\,w^{-1}dw$ and

$$a_k = \frac{1}{2\pi\mathrm{i}}\oint_{|w|=1} \tilde g(w)\,w^{-k-1}\,dw. \tag{S10}$$

Deforming the contour to $|w| = \eta$ with $\rho_{\mathrm{FE}}^{-1} < \eta < \rho_{\mathrm{FE}}$ yields the Cauchy estimate

$$|a_k| \le B\,\eta^{-|k|} \qquad (k \in \mathbb{Z}). \tag{S11}$$

Taking the limit $\eta \to \rho_{\mathrm{FE}}$ for $k \ge 0$ and $\eta \to \rho_{\mathrm{FE}}^{-1}$ for $k \le 0$ then implies

$$|a_k| \le B\,\rho_{\mathrm{FE}}^{-|k|}. \tag{S12}$$

Summing the geometric tails,

$$\sum_{|k|>d} |a_k| \le 2B \sum_{k=d+1}^{\infty} \rho_{\mathrm{FE}}^{-k} = \frac{2B\,\rho_{\mathrm{FE}}^{-(d+1)}}{1-\rho_{\mathrm{FE}}^{-1}}. \tag{S13}$$

Since $g_{\mathrm{ext}} = g$ on $I \subset [c - L_{\mathrm{eff}}, c + L_{\mathrm{eff}}]$, the restriction to I gives $\|g - g_{(d)}^{\mathrm{FE}}\|_I \le \|g_{\mathrm{ext}} - g_{(d)}^{\mathrm{FE}}\|_\infty$, which establishes the stated bound on d.

For the asymptotic, note that $B \le e^{\Delta t\|f\|_{\mathcal{S}_\sigma}}$ and $L_{\mathrm{eff}}/(\pi\sigma) = \tau h/(\pi\sigma)$ are both constants once the physical parameters $(\Delta t, f, h, \tau, \sigma)$ are fixed. The degree bound then reduces to $d = \mathcal{O}(\ln \varepsilon^{-1})$. □

If f extends to an entire function (e.g. polynomials, Morse potentials, trigonometric functions), then $g = e^{\mathrm{i}\Delta t f}$ is itself entire and one may take g_{ext} to be any smooth $2L_{\mathrm{eff}}$-periodic extension; in this case σ can be made arbitrarily large (limited only by the growth of B). When f has singularities in the complex plane, σ is bounded by the distance from I to the nearest singularity of f.

For physically relevant potentials that are entire, e.g., polynomials, Morse, trigonometric functions, the strip half-width σ can be taken as large as the growth of $B = e^{\Delta t \|f\|_{\mathcal{S}_\sigma}}$ permits. In particular, choosing $\sigma = L_{\mathrm{eff}} = \tau h$ gives $\rho_{\mathrm{FE}} = e^{\pi} \approx 23.14$, and the truncation degree simplifies to $d = \mathcal{O}(\ln(1/\varepsilon))$ up to absolute constants. If $1 < \rho_{\mathrm{FE}} < 2$, retain the prefactor $(1 - \rho_{\mathrm{FE}}^{-1})^{-1}$ in the tail bound; this does not arise under $\sigma = L_{\mathrm{eff}}$.

a. Practical implementation. Lemma 2 bounds the *ideal* truncation error under the assumption that the exact Fourier-extension coefficients $\{a_k\}$ are known. In practice, the extension g_{ext} is not available in closed form; instead, one approximates the coefficients from M sample values $\{g(x_j)\}_{j=1}^{M}$ on I by solving the overdetermined system

$$\sum_{|k|\le d} \hat{a}_k \, e^{\mathrm{i}\frac{\pi k}{L_{\mathrm{eff}}}(x_j - c)} \;\approx\; g(x_j), \qquad j = 1, \dots, M,$$

in the least-squares sense. The resulting Fourier-extension matrix is typically ill-conditioned [10], and the numerical coefficients $\hat{a}_k$ are obtained via SVD-based Tikhonov regularization [11]. Consequently the total approximation error decomposes as

$$\|g - g^{\mathrm{FE}}_{\mathrm{num}}\|_I \;\le\; \underbrace{\|g - g^{\mathrm{FE}}_{(d)}\|_I}_{\text{truncation (Lemma 2)}} \;+\; \underbrace{\|g^{\mathrm{FE}}_{(d)} - g^{\mathrm{FE}}_{\mathrm{num}}\|_I}_{\text{fitting \& conditioning}} .$$

Moreover, for the GQSP inverse solver the Laurent polynomial must satisfy $\|P\|_{\mathbb{T}} \le 1 - \eta$ on the full unit circle $\mathbb{T}$, not merely on the physical domain I. Since the Fourier-extension polynomial can grow outside I, a uniform rescaling $\hat{a}_k \mapsto \hat{a}_k \cdot (1-\eta)/\|P\|_{\mathbb{T}}$ is applied whenever $\|P\|_{\mathbb{T}} > 1 - \eta$. This admissibility scaling introduces an additional multiplicative factor that is not captured by the ideal truncation bound.

Finally, the GQSP phase factors are recovered from the Laurent polynomial via the inverse nonlinear fast Fourier transform on SU(2) [12]. Although this inverse map is exact in infinite precision, finite-precision arithmetic introduces an error amplified by at most a $\mathrm{poly}(d)$ factor. The total implementation error therefore satisfies

$$\delta_{\mathrm{total}} \;\le\; \underbrace{C_1 \, \rho_{\mathrm{FE}}^{-d}}_{\text{truncation}} \;+\; \underbrace{C_2 \, \mathrm{poly}(d) \, \varepsilon_{\mathrm{coeff}}}_{\text{GQSP inverse}},$$

where $\varepsilon_{\mathrm{coeff}}$ aggregates the FE fitting and admissibility-scaling errors. Because $\mathrm{poly}(d) \ll \rho_{\mathrm{FE}}^{d}$ for any $\rho_{\mathrm{FE}} > 1$, the exponential convergence $\delta = \mathcal{O}(e^{-\alpha d})$ with $\alpha = \ln \rho_{\mathrm{FE}} = \pi\sigma / L_{\mathrm{eff}}$ is preserved through the GQSP inverse step, provided the coefficient-level error $\varepsilon_{\mathrm{coeff}}$ is controlled by sufficient regularization.

In our numerical experiments, we do not use the analytic estimate for d directly; instead, the parameters (τ, d, M) are selected by sweeping over candidate values and retaining the configuration whose phase error on a dense evaluation grid falls below a prescribed tolerance.

D. Off-diagonal anharmonic coupling from diagonal OQ-GQSP

When the off-diagonal coupling is itself anharmonic, i.e. $(|n\rangle\langle m| + |m\rangle\langle n|) \otimes f_{nm,r}(\hat{Q}_r)$ with a nonlinear $f_{nm,r}$, the corresponding propagator can be reduced to diagonal state-dependent phase gates

by diagonalizing the electronic part. Define the pair-Pauli operators on the $\{|n\rangle, |m\rangle\}$ subspace,

$$X_{nm} = |n\rangle\langle m| + |m\rangle\langle n|, \quad Y_{nm} = -i\,|n\rangle\langle m| + i\,|m\rangle\langle n|, \quad Z_{nm} = |n\rangle\langle n| - |m\rangle\langle m|, \tag{S14}$$

and the two-level Givens rotation $R_y^{(nm)}(\theta) := \exp[-i\theta Y_{nm}/2]$. Since $X_{nm} = R_y^{(nm)}(\pi/2)\, Z_{nm}\, R_y^{(nm)}(-\pi/2)$, the off-diagonal propagator factorizes exactly as

$$\mathrm{e}^{-i\Delta t\, X_{nm}\otimes f_{nm,r}(\hat{Q}_r)} = R_y^{(nm)}\Big(\frac{\pi}{2}\Big)\ \mathrm{e}^{-i\Delta t\, P_n\otimes f_{nm,r}(\hat{Q}_r)}\ \mathrm{e}^{+i\Delta t\, P_m\otimes f_{nm,r}(\hat{Q}_r)}\ R_y^{(nm)}\Big(-\frac{\pi}{2}\Big), \tag{S15}$$

where $P_k = |k\rangle\langle k|$ and we used $Z_{nm} = P_n - P_m$ with $[P_n \otimes f,\, P_m \otimes f] = 0$. Each exponential factor is a diagonal state-dependent nonlinear bosonic phase gate compilable by OQ-GQSP (Lemma 1), and the Givens rotations $R_y^{(nm)}$ are constant-overhead electronic gates acting only on qubits n and m in the inverted unary encoding. Thus each off-diagonal anharmonic propagator requires two diagonal OQ-GQSP sequences plus $\mathcal{O}(1)$ electronic gates, with a combined error bounded by $2\varepsilon_{\mathrm{diag}}$ (the per-block OQ-GQSP synthesis error) and success probability $(1-\delta)^4$, where $\delta = \|G(\hat{U})\|^2 \ll 1$ is the leakage weight defined in Lemma 1.

IV. REFERENCE HIERARCHY BEHIND FIGURE 7

For the reduced two-mode Hamiltonian used in Figure 7 of the main text, it is helpful to distinguish four layers of dynamics. The formal target is the reduced-model propagator $U(t) = e^{-iHt}$, where H acts on the bosonic Hilbert space of the $\{\nu_{21}, \nu_{26}\}$ model. This object is not computed directly in closed form. The auxiliary "diag" curves instead denote exact propagation after projection onto a fixed truncated bosonic Fock basis, $\tilde{H}_{\mathrm{Fock}} = P_K H P_K$, with $K = 30$ in the numerical experiments shown in Figure 7. The "diag + Trotter" and compiled OQ-GQSP curves inherit the same first-order product formula on top of this fixed truncated-Fock representation, so their mutual discrepancy isolates the compilation error of the nonlinear diagonal propagators. The no-Trotter "diag" curves instead propagate the same projected Hamiltonian $\tilde{H}_{\mathrm{Fock}}$ without a product formula and therefore isolate the Trotter contribution within the fixed $K = 30$ model. By contrast, MCTDH is evaluated in an independent time-dependent variational representation using a harmonic-oscillator discrete-variable representation (HO-DVR) primitive basis with single-particle functions (SPFs) and is therefore used only as an external classical benchmark, not as the exact reduced-model propagator.

Figure S3 clarifies the three distinct error scales behind the main-text benchmark. First, the OQ-GQSP curves remain nearly coincident with the "diag + Trotter" target: the representative mismatch $|P_{\mathrm{OQ}} - P_{\mathrm{diag+Trotter}}|$ peaks at only 2.94×10^{-3} in panel (a) and 1.36×10^{-4} in panel (b). Second, the Trotter contribution inside the fixed truncated-Fock model is substantially larger, with $|P_{\mathrm{diag+Trotter}} - P_{\mathrm{diag}}|$ peaking at 3.28×10^{-2} near 22.5 fs in panel (a) and 1.51×10^{-2} near 7.5 fs in panel (b). Third, the independent MCTDH benchmark is not numerically identical to the projected truncated-Fock model but still tracks the no-Trotter "diag" curves closely at late times: $|P_{\mathrm{MCTDH}} - P_{\mathrm{diag}}|$ peaks at 1.35×10^{-2} in panel (a) and 7.19×10^{-4} in panel (b), while the final-time discrepancies are only 7.25×10^{-4} and 5.42×10^{-5}, respectively. Because the MCTDH trajectories are propagated in a natural-HO-DVR/SPF representation rather than in the fixed truncated-Fock basis, exact coincidence with the no-Trotter curves is not expected a priori even when both are derived from the same reduced Hamiltonian. The somewhat larger excursion in panel (a) is consistent with that subspace being more representation-sensitive, since it combines the large initial ν_{21} displacement, an additional Q_{21} off-diagonal coupling, and the more asymmetric D_1/D_3 Morse pair. Taken together,

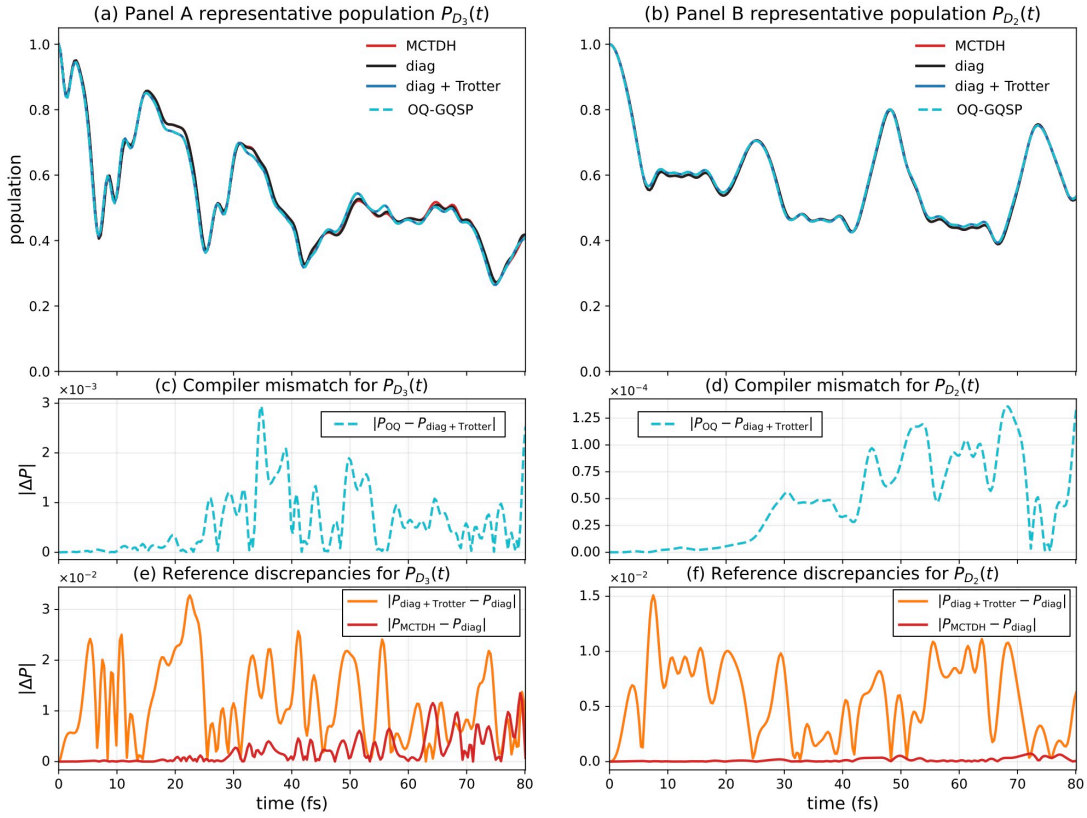

FIG. S3. Reference hierarchy associated with Figure 7 of the main text. The upper row shows representative populations $P_{D_3}(t)$ for panel (a) and $P_{D_2}(t)$ for panel (b), comparing OQ-GQSP (cyan dashed), diag + Trotter (blue), diag (black), and the independent natural-HO-DVR MCTDH benchmark (red). The middle row isolates the compiler mismatch $|P_{\mathrm{OQ}} - P_{\mathrm{diag+Trotter}}|$, which remains much smaller than the other discrepancies throughout the full 80.1 fs window. The lower row compares $|P_{\mathrm{diag+Trotter}} - P_{\mathrm{diag}}|$ and $|P_{\mathrm{MCTDH}} - P_{\mathrm{diag}}|$, separating the Lie-Trotter contribution inside the projected truncated-Fock model from the residual difference between the fixed truncated-Fock and HO-DVR/SPF realizations of the same reduced dynamics.

Fig. S3 shows a clear hierarchy in which the OQ-GQSP compilation error is the smallest scale, the Lie-Trotter contribution is the dominant internal approximation within the projected $K = 30$ model, and the remaining MCTDH difference reflects the use of an independent HO-DVR/SPF realization of the same reduced dynamics.

REFERENCES

[1] M. Assmann, H. Köppel, and S. Matsika, Photoelectron spectrum and dynamics of the uracil cation, J. Phys. Chem. A **119**, 866 (2015).

[2] P. Vindel-Zandbergen, S. Matsika, and N. T. Maitra, Exact-factorization-based surface hopping for multistate dynamics, J. Phys. Chem. Lett. **13**, 1785 (2022).

[3] O. Katz, M. Cetina, and C. Monroe, Programmable n-body interactions with trapped ions, PRX Quantum **4**, 030311 (2023).

[4] A. Eickbusch, V. Sivak, A. Z. Ding, S. S. Elder, S. R. Jha, J. Venkatraman, B. Royer, S. M. Girvin, R. J. Schoelkopf, and M. H. Devoret, Fast universal control of an oscillator with weak dispersive coupling to a qubit, Nat. Phys. **18**, 1464 (2022).

[5] D. Leibfried, R. Blatt, C. Monroe, and D. Wineland, Quantum dynamics of single trapped ions, Reviews of Modern Physics **75**, 281 (2003).

[6] S. Krastanov, V. V. Albert, C. Shen, C.-L. Zou, R. W. Heeres, B. Vlastakis, R. J. Schoelkopf, and L. Jiang, Universal control of an oscillator with dispersive coupling to a qubit, Physical Review A **92**, 040303 (2015).

[7] D. Motlagh and N. Wiebe, Generalized quantum signal processing, PRX Quantum **5**, 020368 (2024).

[8] L. N. Trefethen, *Approximation Theory and Approximation Practice, Extended Edition* (SIAM, 2019).

[9] D. Huybrechs, On the Fourier extension of nonperiodic functions, SIAM Journal on Numerical Analysis **47**, 4326 (2010).

[10] B. Adcock, D. Huybrechs, and J. Martín-Vaquero, On the numerical stability of Fourier extensions, Foundations of Computational Mathematics **14**, 635 (2014).

[11] B. Adcock and J. Ruan, Parameter selection and numerical approximation properties of Fourier extensions from fixed data, Journal of Computational Physics **273**, 453 (2014).

[12] H. Ni, R. Sarkar, L. Ying, and L. Lin, Inverse nonlinear fast fourier transform on su(2) with applications to quantum signal processing (2025), arXiv:2505.12615 [quant-ph].